Chemical Science

ROYAL SOCIETY OF CHEMISTRY

EDGE ARTICLE

View Article Online
View Journal | View Issue

Check for updates

Cite this: *Chem. Sci.*, 2026, **17**, 4669

All publication charges for this article have been paid for by the Royal Society of Chemistry

Pyrene-based conjugated porous polymers as photocatalysts for oxidative cycloaddition of phenols

Shuili Liu,[ab] Xingji Liu,[b] Xiu Gu,[b] Shicheng Dong,[b] Nan Huang,*[b] Lei Shi *[a] and Jun Jiang *[b]

Received 14th November 2025
Accepted 9th December 2025

DOI: 10.1039/d5sc08900j

rsc.li/chemical-science

Photocatalytic heterogeneous organic transformation represents an ecofriendly and sustainable method for addressing persistent energy and environmental challenges. Conjugated porous polymer (CPP)-based materials have recently emerged as promising photocatalysts for diverse organic transformations, offering a sustainable alternative to homogeneous systems reliant on precious inorganic or organic dyes. Herein, we designed two pyrene-based CPPs for visible-light photocatalysis, featuring fluoro- or methyl-substituted fluorenes as distinct units. These CPPs act as metal-free, visible-light-activated, reusable heterogeneous photocatalysts for synthesizing benzofused oxa-heterocycles *via* photooxidized [4 + 2] and [3 + 2] cycloadditions of phenols with alkenes. Notably, DFT calculations demonstrate that the fluoro-block CPP with its larger dipole moment can achieve more efficient photoinduced charge separation, due to the stronger electron-attractive force. Consequently, FF-Py-CPP exhibited superior photocatalytic activity compared to MF-Py-CPP, achieving excellent yields, high diastereoselectivity, and good recyclability in the syntheses of chromanes and dihydrobenzofuran.

Introduction

Photocatalysis leverages solar energy to overcome thermodynamic barriers, enabling efficient chemical reactions under mild conditions, thereby significantly reducing reliance on traditional energy sources and attracting considerable research interest.[1–5] Over the past decades, organic semiconductor materials have attracted substantial attention across diverse fields including energy,[6] sensing,[7] and biomedical engineering[8] with their application as photocatalysts in organic transformations being extensively investigated.[9] Nevertheless, these materials often suffer from inherent limitations like narrow light absorption spectra, photocorrosion susceptibility, demanding structural modification requirements, and rapid recombination of photogenerated charge carriers.[10] These shortcomings frequently result in inadequate photocatalytic performance. To address these challenges, reticular materials featuring tunable electronic structures and enhanced charge transport have emerged as promising metal-free alternatives to conventional catalysts, combining low toxicity with exceptional stability and reusability.[11–13]

Recently, porous organic polymers (POPs), including covalent organic frameworks (COFs), covalent triazine-based frameworks (CTFs), hypercrosslinked polymers (HCPs), and conjugated porous polymers (CPPs), have gained significant attention as effective photocatalysts for a variety of organic reactions.[14–17] Among them, CPPs are regarded as a new class of promising photocatalysts due to the extended π-electron systems, diverse synthetic strategies, abundance of building blocks, and tunable band gaps.[18,19] Recent advances have established diverse elegant strategies for structuring CPPs and demonstrated their significant potential in photocatalysis, particularly in hydrogen evolution,[20] selective oxidation of sulfides,[21] molecular oxygen activation,[22] photocatalytic oxidative coupling of amines,[23] and oxidative carbon-hydrogen functionalizations.[24] Despite these advances, additional progress in the development of robust and effective CPPs for complex organic transformations is still urgently required.

Advances in molecular building blocks and integration techniques have greatly facilitated recent progress, enabling precise structural modification and functionalization of CPPs to overcome the rapid recombination of photogenerated charge carriers.[25–27] One viable approach is the attractive dipole moment of organic semiconducting molecules, which promotes spin-orbital interactions and consequently enhances photoinduced charge separation.[28–31] However, designing CPPs with optimized dipole moments presents a significant challenge. Fortunately, fluorination has emerged as a key approach to tuning energy levels and optical properties while promoting

---

[a] School of Chemistry, Dalian University of Technology, Dalian, 116024, China. E-mail: shileichem@dlut.edu.cn

[b] School of Chemistry and Chemical Engineering, Guangxi Colleges, Universities Key Laboratory of Applied Chemistry Technology and Resource Development, Guangxi University, Nanning, 530004, China. E-mail: jiangjun@gxu.edu.cn

charge separation.[32,33] Therefore, introducing fluoro-substituted units into CPPs achieves exceptional charge transport and stability, as the enhanced dipole moment generates a stronger built-in electric field, which in turn facilitates efficient charge separation and transfer. In this context, fluorene is not only an essential charge-transport motif, but its C(sp^3)-functionalization also enables tunable monomer properties, providing a platform for the design of CPPs *via* fluorination.[34–36] On the other hand, pyrene, as a polycyclic aromatic hydrocarbon, facilitates smooth charge carrier separation and transport through its fully π-conjugated configuration.[37–40] This enhances the degree of conjugation of CPPs, intensifies intramolecular charge transfer and improves the efficiency of carrier separation.[41–43] Consequently, we expect that using the side chain modification of fluorene to enhance the dipole moment and work in synergy with the π-electron conjugated network of the macromolecular framework will enhance the photoinduced charge separation of CPPs. These advantages motivate further exploration of the relationship between side-chain modification strategies in CPPs and their photocatalytic performance, to advance applications in complex organic transformations.[44]

Ortho-quinone methides (*o*-QMs) are highly reactive organic intermediates that are typically employed as dienes in [4 + 2] cycloadditions with olefins to construct chromanes in an atom-economic manner.[45–49] However, the range of substrates that can be used in current visible-light-induced catalytic approaches for this transformation is limited to those with activated leaving groups or conjugated structures, such as *ortho*-sulfomethylphenol and *ortho*-propenylphenol.[50–53] Recently, *ortho*-alkylarenols have emerged as suitable *o*-QM precursors offering high atom economy and sustainability.[54–56] Their low oxidation potential allows visible light activation of the benzyl C(sp^3)–H bond for *in situ* generation of *o*-QMs. To the best of our knowledge, heterogeneous photocatalysis for the [4 + 2] cycloaddition of *o*-QMs has not been developed.[57,58] Therefore, developing metal-free, recyclable, and low-energy consumption heterogeneous photocatalytic systems for the efficient oxidative [4 + 2] cycloadditions of *ortho*-alkylarenols with olefins under visible light irradiation is highly desirable.

Herein, we designed two CPP photocatalysts (FF-Py-CPP and MF-Py-CPP) featuring fluoro or methyl substituents at the bridgehead carbon of the 2,7-dibromo-9*H*-fluorene unit to probe substituent effects on photocatalytic activity. Intriguingly, FF-Py-CPP exhibited broad substrate scope as a visible-light-activated heterogeneous photocatalyst, achieving high conversion and stereoselectivity in visible-light-driven oxidative cycloadditions of phenols with olefins. We demonstrated that introducing strongly electron-withdrawing fluoro groups at the 2,7-dibromo-9*H*-fluorene unit promotes π-electron delocalization through an over-conjugated backbone, thereby enhancing the dipole moment and facilitating photoinduced charge separation. Notably, these finely designed CPPs showed excellent stability, photoelectric response capability, and reusability, which make these materials economical, sustainable, and eco-friendly photocatalysts. This study provides important insights into the molecular design of CPPs for photocatalytic applications at the atomic scale.

Results and discussion

Designed synthesis and structural characterization

The polymer photocatalysts FF-Py-CPP and MF-Py-CPP were synthesized by Pd-catalyzed Suzuki polymerization of 1,3,6,8-tetrakis(4,4,5,5-tetramethyl-1,3,2-dioxaborolan-2-yl)pyrene with 2,7-dibromo-9,9-dimethyl-9*H*-fluorene or 2,7-dibromo-9,9-difluoro-9*H*-fluorene, respectively (Scheme 1, see details in the SI). To characterize the chemical and morphological properties of these CPPs, spectroscopic and analytical methods were carried out. Fourier-transform infrared (FT-IR) spectra were recorded to identify the characteristic functional groups in the two pyrene-

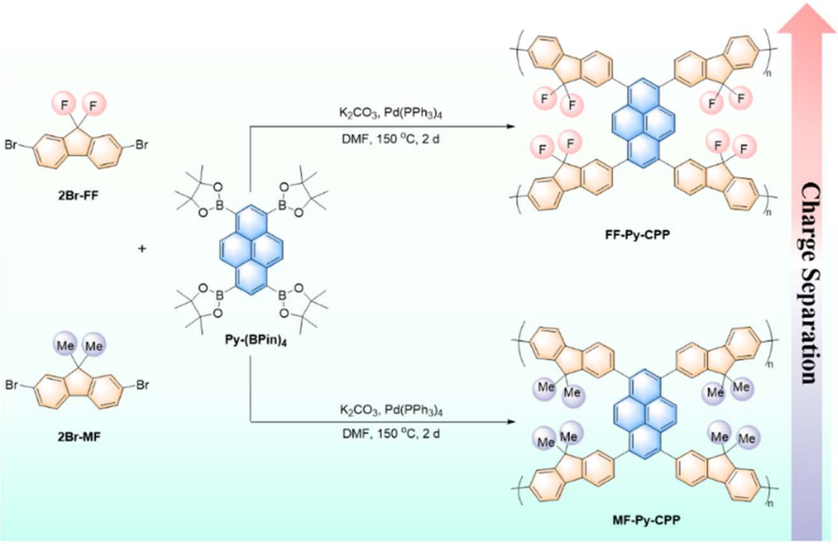

Scheme 1 The preparation routes for FF-Py-CPP and MF-Py-CPP polymers.

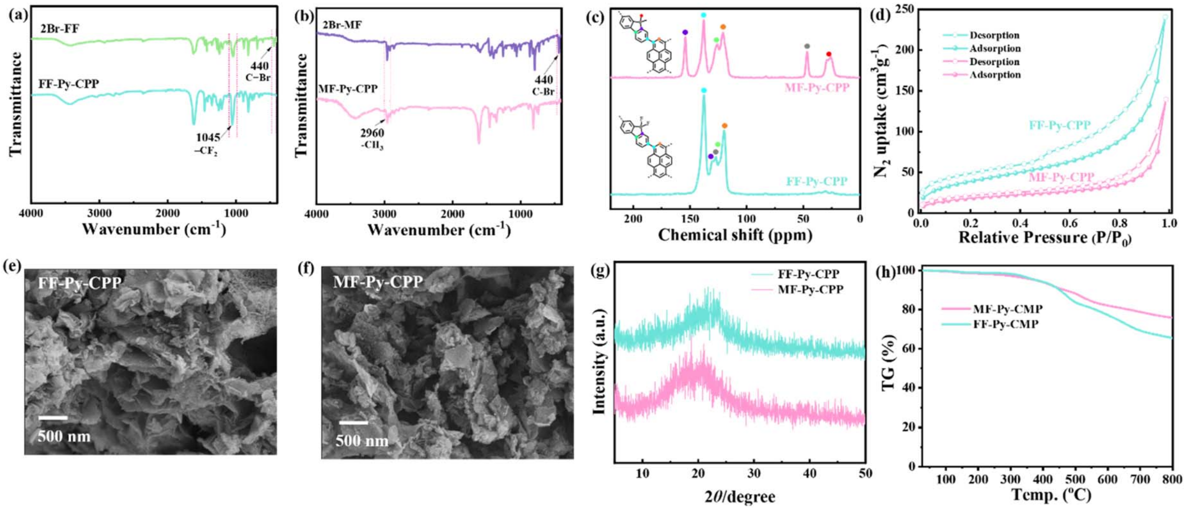

Fig. 1 (a) FTIR spectra of 2Br-FF and FF-Py-CPP. (b) FTIR spectra of 2Br-MF and MF-Py-CPP. (c) Solid-state ^{13}C NMR spectra of FF-Py-CPP and MF-Py-CPP. (d) N_2 adsorption/desorption isotherms of FF-Py-CPP and MF-Py-CPP. (e) SEM image of FF-Py-CPP. (f) SEM image of MF-Py-CPP. (g) Powder X-ray diffraction (PXRD) patterns of FF-Py-CPP and MF-Py-CPP. (h) TGA of FF-Py-CPP and MF-Py-CPP under a N_2 atmosphere with a heating rate of 10 °C min^{-1}.

based CPPs (Fig. 1a and b). FT-IR analysis revealed a distinct stretching vibration at 1045 cm^{-1} for the $–CF_2$ group in the 2Br-FF monomer, while the 2Br-MF monomer showed a characteristic stretching peak at 2960 cm^{-1} for the $–CH_3$ group in the fluorene moiety. More importantly, the characteristic peak at 440 cm^{-1} originating from the C–Br stretching vibration decreased markedly in the FT-IR spectra of both pyrene-based CPPs, indicating successful formation of the sp^2 carbon framework *via* the Suzuki cross-coupling reaction.[59] As shown in the solid-state ^{13}C NMR spectrum (Fig. 1c), the peaks corresponding to aromatic carbons appeared consistently between 100 and 155 ppm in these two CPPs, which could be assigned to the aromatic carbons in pyrene and fluorene moieties. The typical peak of the $–CF_2$ carbon in FF-Py-CPP overlaps with aromatic ring carbon signals, appearing as a broadened peak at 120 ppm, whereas the quaternary methylene bridge carbon peak in MF-Py-CPP appears at 46 ppm, and the peak for methyl carbons appeared in the high field at about 25 ppm. All these data authenticate the robust couplings between Py-(Bpin)$_4$ and 2Br-FF or 2Br-MF in forming the two CPPs.

The porous features of CPPs were examined using N_2 sorption at 77 K (Fig. 1d). The Brunauer–Emmett–Teller (BET) and Langmuir surface areas of FF-Py-CPP and MF-Py-CPP were calculated to be 146 and 69 m^2 g^{-1}, respectively. Obviously, the rapid increase in adsorbed quantity at $0.8 < P/P_0 < 1.0$ illustrated the existence of abundant mesopores and macropores in both the pyrene-based CPPs. This conclusion was further substantiated by pore size distributions based on the nonlocal density functional theory (NLDFT) model (Fig. S1). Furthermore, scanning electron microscopy (SEM) and transmission electron microscopy (TEM) reveal the morphology of FF-Py-CPP and MF-Py-CPP. As shown in Fig. 1e and f, both CPPs displayed rather rough surfaces and similar structures of pore-like morphologies. No obvious lattice diffraction fringes are observed in all high-resolution TEM images of both CPPs, demonstrating the amorphous structures of the CPPs (Fig. S2). The broad peaks shown in powder X-ray diffraction patterns of both CPPs also supported this result (Fig. 1g). The elemental mapping indicates the presence of C and O elements in both CPPs and the F element in FF-Py-CPP with fluorine atoms. Meanwhile, the distribution of each element is uniformly distributed. Similarly, the XPS surveys of the two CPPs also confirmed this result (Fig. S3a and b). The high-resolution C 1s XPS of FF-Py-CPP shows two peaks at 284.8, and 292.0 eV, corresponding to C═C/C–C, and $–CF_2$, respectively (Fig. S3c). In addition, a signal at 688.0 eV is observed in the F 1s spectrum (Fig. S3d). The high-resolution C 1s XPS of MF-Py-CPP shows a peak at 284.8 corresponding to C═C/C–C (Fig. S3e). Finally, thermogravimetric analysis (TGA) revealed that they possessed favorable stability up to 400 °C with only 5–10% weight loss under a nitrogen atmosphere (Fig. 1h).

Photoelectric properties

To evaluate the photocatalytic activity of these pyrene-based CPPs, a series of optical and electronic properties were characterized. Ultraviolet/visible (UV/vis) diffuse reflectance (DR) spectra (Fig. 2a) showed that CPPs responded to light with a broad range of 200–800 nm and appeared as yellow powders. The maximum absorption regions of both FF-Py-CPP and MF-Py-CPP are concentrated at 250–430 nm. Notably, FF-Py-CPP showed an obvious red-shifted absorption onset at around 20 nm compared with MF-Py-CPP, suggesting enhanced conjugation along its polymer chain. This might be due to the fact that fluorine atoms reduce steric hindrance *versus* methyl groups, thereby improving the backbone planarity and π-electron delocalization throughout the polymer skeleton.[60] The optical band gaps (E_g) were estimated to be 2.25 eV for the FF-Py-CPP and 2.35 eV for the MF-Py-CPP through Tauc plots (Fig. 2b).

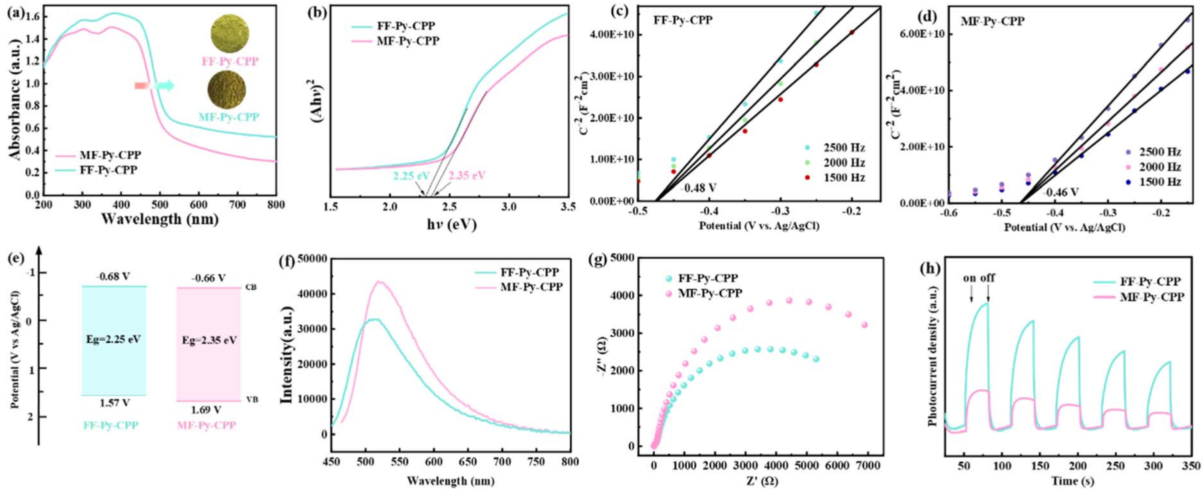

Fig. 2 (a) The solid-state UV-visible spectra (inset: photographs of the polymers). (b) The Tauc plots. (c) The Mott–Schottky analysis for FF-Py-CPP. (d) The Mott–Schottky analysis for MF-Py-CPP. (e) Electronic band structures. (f) Photoluminescence spectra of CPPs. (g) The Nyquist plots of EIS. (h) Transient photocurrents of FF-Py-CPP and MF-Py-CPP.

Moreover, the characteristic of n-type semiconductors for FF-Py-CPP and MF-Py-CPP was revealed by the positive slopes presented in their Mott–Schottky plots (Fig. 2c and d). Electrochemical Mott–Schottky measurements were performed to assess the conduction band (CB) positions; the positive slope of the M–S plots is indicative of n-type semiconductor behavior. Consequently, the CB positions of FF-Py-CPP and MF-Py-CPP were determined to be −0.48 eV and −0.46 eV (*vs.* Ag/AgCl), respectively. In conjunction with the band gaps derived from UV/Vis absorption, the corresponding valence band (VB) edges were calculated and are illustrated in Fig. 2e. The narrow distribution of band gaps observed in the two CPPs suggested their potential as promising candidates for use as photosensitizers. No obvious difference in the valence band was observed between the two polymers, possibly due to their similar chemical components. Moreover, the steady-state photoluminescence (PL) spectrum of FF-Py-CPP showed lower intensity compared to that of MF-Py-CPP at ~518 nm (Fig. 2f). This reflected that FF-Py-CPP with the incorporation of fluoro groups into the CPP backbone had a lower probability of electron–hole recombination than MF-Py-CPP, which may be conducive to improving the separation efficiency of photogenerated charge.[56] Additionally, FF-Py-CPP (τ_{ave} = 2.41 ns) showed the longest lifetimes in time-resolved fluorescence decay measurements compared to MF-Py-CPP (τ_{ave} = 2.37 ns), suggesting more efficient electron–hole separation (Fig. S4). In the Nyquist plots, the smaller semicircular radius of FF-Py-CPP elucidated the decreased internal resistance and increased efficiency for the charge transfer (Fig. 2g). Additionally, photocurrent measurement showed a much stronger photocurrent in FF-Py-CPP compared to MF-Py-CPP (Fig. 2h). This implies that more photoinduced charge carriers are generated in FF-Py-CPP during photocatalysis, due to its broader light absorption region and the narrower band gap relative to MF-Py-CPP. Notably, the photocurrent responses of both CPPs have a slow downhill process, which is caused by the rapid accumulation of charges on the sample surface under light excitation.[61]

Next, we employed density functional theory (DFT) calculation to examine the electronic structural characteristics of FF-Py-CPP and MF-Py-CPP. The optimized structures of both CPPs model units exhibit a clear separation of electronic states. The HOMO's electron density is mainly localized on the pyrene part, whereas the LUMO is delocalized across the whole model unit (Fig. 3a). Additionally, the dipole moments of the CPPs were calculated, showing that FF-Py-CPP has a higher dipole moment (7.49 D) than MF-Py-CPP (1.45 D) (Fig. 3b). Correspondingly,

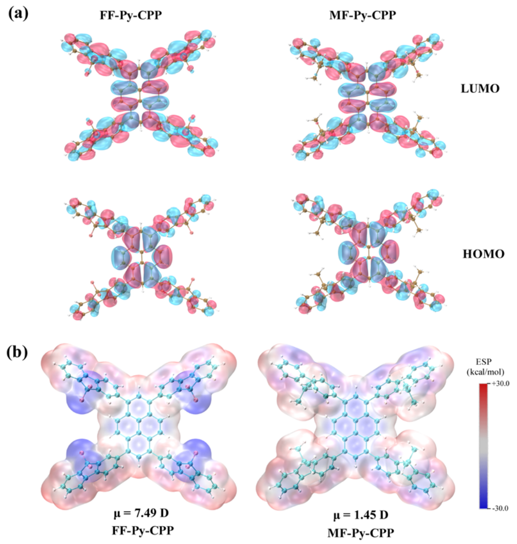

Fig. 3 (a) DFT calculated frontier molecular orbitals for FF-Py-CPP and MF-Py-CPP. (b) The ESP surface maps for the optimized structures of FF-Py-CPP and MF-Py-CPP. Regions with electronegativity attract electrons, and regions with electropositivity repel electrons. The isosurface 0.01 a.u. is plotted.

a larger dipole moment is beneficial for promoting charge transfer.

Photocatalytic cycloaddition reactions

Over the past decades, *o*-QMs have been widely used as reactive synthetic building blocks for the construction of natural products and pharmaceutical compounds. Specifically, *o*-QMs can act as heterodienes in inverse electron-demand hetero-Diels–Alder (IED-HDA) reactions to construct six-membered heterocycles.[62,63] In this context, we surveyed the visible-light-induced IED-HDA reaction of 2-benzylphenol **1a** with *trans*-anethole **2a**, catalyzed by FF-Py-CPP and MF-Py-CPP under blue LED irradiation. Upon systematic optimization (Table S1), we found that the reaction afforded 74% isolated yield with excellent diastereoselectivity (>20 : 1 dr) under the following conditions: FF-Py-CPP as the photocatalyst, $(NH_4)_2S_2O_8$ as the additive, TFE as the solvent, Na_2HPO_4 as the base, and irradiation with 25 W blue LEDs (400–410 nm) for 24 h at ambient temperature (Table 1, entry 1). A series of control experiments were conducted without FF-Py-CPP, light or $(NH_4)_2S_2O_8$, and the desired product could not be detected, demonstrating their essential role in this transformation (Table 1, entries 2–4). The reaction occurred smoothly without Na_2HPO_4, but the yield decreased to 65%, indicating that the base is beneficial for deprotonation to generate *o*-QM (Table 1, entry 5). Furthermore, a light on/off experiment was performed over time (Fig. S5), indicating that continuous light is essential for this reaction process, confirming the photoredox cycle's crucial role in sustaining the catalytic system. The change of oxidants or solvents led to lower yields (Table 1, entries 6–10). To further investigate the optimal reaction conditions, the model reaction was conducted under different light intensities and wavelengths (Table 1, entries 11–16). However, none of these variations afforded a better yield than the conditions employing 400–410 nm (25 W) LEDs. Reducing the catalyst loading to 1 mol% decreased the product yield significantly (Table 1, entry 17). While increasing the loading to 3.5 mol%, 4 mol%, 4.5 mol% and 5 mol% provided yields comparable to those achieved with 3 mol% (Table S1, entries 21–24). In addition, replacing the photocatalyst FF-Py-CPP with MF-Py-CPP resulted in significantly reduced yield (Table 1, entry 18). This difference in catalytic performance may be attributed to their distinct optoelectronic properties, such as photocurrent response and electrochemical impedance (EIS). Finally, monomers 2Br-FF and Py-$(Bpin)_4$ were used in this reaction as photocatalysts instead of FF-Py-CPP under the standard conditions, and no desired product was obtained (Table 1, entries 19 and 20). This result indicates that the polymer plays a crucial role in enhancing catalytic activity, rather than acting as an independent fragment. To further understand the structural advantages of the polymer, substrate adsorption experiments were carried out. In these experiments, an equimolar solution of **1a** and **2a** (20 mmol L^{-1} each) was used, and the adsorption capacities of FF-Py-CPP for **1a** and **2a** were found to be 0.5 mmol g^{-1} and 0.6 mmol g^{-1}, respectively (Fig. S6). These results indicated that the active sites within the catalyst are readily accessible to the substrates.

Table 1 Reaction optimization

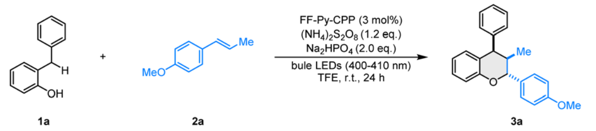

Entry	Variation from the standard conditions	Yield[b] (%)
1	Standard condition[a]	74
2	No FF-Py-CPP	NR
3	No light (dark)	NR
4	No $(NH_4)_2S_2O_8$	NR
5	No Na_2HPO_4	65
6	^{t}BuOOH instead of $(NH_4)_2S_2O_8$	NR
7	BPO instead of $(NH_4)_2S_2O_8$	Trace
8	TBHP instead of $(NH_4)_2S_2O_8$	24
9	MeOH instead of TFE	31
10	CH_3CN instead of TFE	Trace
11	Under 360–370 nm 25 W LEDs	50
12	Under 400–410 nm 25 W LEDs	74
13	Under 460–470 nm 25 W LEDs	48
14	Under 520–530 nm 25 W LEDs	23
15	Under 400–410 nm 5 W LEDs	65
16	Under 400–410 nm 45 W LEDs	72
17	1 mol% of FF-Py-CPP instead of 3 mol%	34
18	MF-Py-CPP instead of FF-Py-CPP	32
19	2Br-FF instead of FF-Py-CPP	NR
20	Py-$(Bpin)_4$ instead of FF-Py-CPP	NR

[a] Standard conditions: **1a** (0.20 mmol), **2a** (0.40 mmol), FF-Py-CPP (3 mol%), $(NH_4)_2S_2O_8$ (0.24 mmol), Na_2HPO_4 (0.40 mmol), TFE (1 mL), 400–410 nm 25 W blue LEDs, room temperature, 24 h. [b] Isolated yields.

With the optimized photocatalytic IED-HDA reaction conditions established after extensive experimentation, we systematically investigated diverse substrates to examine the generality of the heterogeneous photocatalyst FF-Py-CPP (Scheme 2). Various 2-benzylphenols **1** bearing electron-donating groups (Me and OMe) on the phenol ring reacted effectively with *trans*-anethole **2a**, affording the anticipated products **3b** and **3c** in good yields (75–77%) with good to excellent diastereoselectivity (10 : 1 – >20 : 1 dr). The structure of **3c** was confirmed through single-crystal X-ray diffraction analysis (Fig. S16). Moreover, **1** bearing methyl and methoxyl groups at the *para*-position of the phenyl ring also proved to be suitable candidates for this transformation, affording products **3d** and **3e** in 62% and 67% yields, respectively. Subsequently, we probed other dienophile styrenes **2**. Electronic properties of substituents exhibited a slight influence on the reaction efficiency, but a significant influence on diastereoselectivity. For example, an electron-neutral substitute (H) gave higher diastereoselectivity than an electron-donating group (OMe) with comparable yields (**3f**, 56%, >20 : 1 dr *vs.* **3h**, 63%, 1 : 1 dr). Furthermore, prop-1-en-2-ylbenzene **2f** also acted as a diene precursor, affording triphenylchroman **3j** in 23% yield with 2 : 1 dr. Notably, this photocatalytic IED-HDA reaction enables late-stage applications of bio-relevant compounds. Styrenes derived from natural products and pharmaceuticals including (+)-menthol **3k**, ibuprofen **3l**, and estrone **3m** were well-tolerated under the

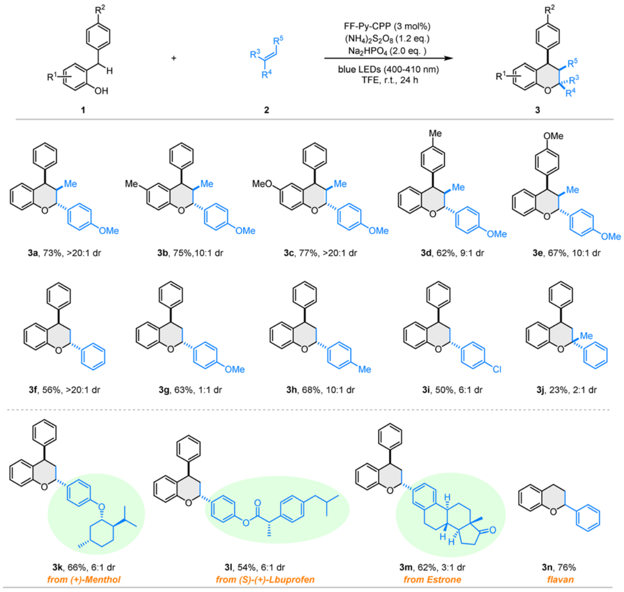

Scheme 2 Substrate range of the visible-light induced [4 + 2] cycloaddition of phenols with olefins catalyzed by FF-Py-CPP. Standard conditions: **1** (0.20 mmol), **2** (0.40 mmol), FF-Py-CPP (3 mol%), $(NH_4)_2S_2O_8$ (0.24 mmol), Na_2HPO_4 (0.40 mmol), TFE (1 mL), 400–410 nm 25 W blue LEDs, room temperature, 24 h. Isolated yields.

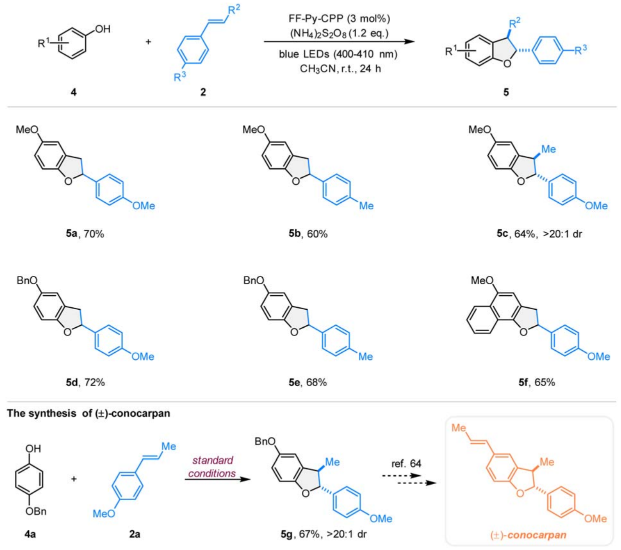

Scheme 3 Substrate range of the visible-light induced [3 + 2] cycloaddition of phenols with olefins catalyzed by FF-Py-CPP. Reaction conditions: **4** (0.20 mmol), **2** (0.40 mmol), FF-Py-CPP (3 mol%), $(NH_4)_2S_2O_8$ (0.24 mmol), CH_3CN (2.0 mL), 400–410 nm 25 W blue LEDs, room temperature, 24 h. Isolated yields.

photooxidation conditions, demonstrating exceptional robustness and versatility. Additionally, flavan derivative **3n** was efficiently constructed *via* photocatalytic HAD reaction in 76% yield from readily available starting materials.

To demonstrate the wider utility of this pyrene-based polymer photocatalyst, we examined the catalytic activity of FF-Py-CPP in the photooxidative [3 + 2] cycloaddition of phenols to synthesize dihydrobenzofuran scaffolds that are commonly found in many important bioactive natural products (Scheme 3).[64–67] Based on the above reaction procedure with modifications, the scope of this photocatalytic system for the synthesis of 2,3-dihydrobenzofuran analogs was explored by varying the phenols **4** and olefins **2**. First, styrenes substituted at the *para*-position with methoxyl and methyl groups reacted smoothly with 4-methoxyphenol **4**, affording the corresponding dihydrobenzofurans in medium to good yields (**5a–5b**). Notably, *trans*-anethole **2a** was also compatible, yielding the target product **5c** in 64% yield with excellent diastereoselectivity (>20 : 1 dr). Next, 4-(benzyloxy)phenol reacted efficiently as the phenol substrate to generate the desired products **5d** and **5e** in 72% and 68% yields. Additionally, 4-methoxynaphthalen-1-ol also proved suitable for this oxidative [3 + 2] cycloaddition to react with **2c**, providing the desired product **5f** in 65% yield. Furthermore, the natural product precursor **5g** of (±)-conocarpan was produced, yielding 67% of the desired product.[64]

In addition to catalytic activity, recyclability represents a crucial parameter for heterogeneous catalysis in practical applications. Therefore, recycling experiments were conducted to evaluate the reusability and stability of FF-Py-CPP. The photocatalyst FF-Py-CPP was readily separated from the reaction mixture *via* centrifugation and subsequently utilized for the next photocatalytic cycles. As can be seen in Fig. S7, no obvious loss in yield was observed after six cycles. It was worth noting that the SEM images (Fig. S8), PXRD (Fig. S9), and IR spectral analysis of FF-Py-CPP after the sixth reaction reflected almost the same spectrum of fresh FF-Py-CPP (Fig. S10).

To systematically understand the reaction mechanism of this photocatalysis process, a number of controlled experiments were performed. The reactions were conducted under the optimized conditions in the presence of 2,2,6,6-tetramethylpiperidinooxy (TEMPO) or 2,6-di-*tert*-butyl-4-methylphenol (BHT) as a radical scavenger (Scheme S1), $AgNO_3$ as an e^- scavenger, and KI as an h^+ scavenger (Fig. 4a). In the presence of TEMPO or BHT, cycloaddition reaction was sharply inhibited or completely quenched, indicating the involvement of a radical process. Similarly, the presence of either $AgNO_3$ or KI inhibited the product formation (23% and 7%, respectively), suggesting that both reductive e^- and oxidative h^+ participate in the photocatalytic process. To more clearly demonstrate the photoexcitation process in the initial stage of the reaction, time-dependent density functional theory (TDDFT) calculations were performed. Calculated energies of the HOMO and LUMO of substrate **1a** and FF-Py-CPP are shown in Fig. 4b. Once FF-Py-CPP is photoexcited, substrate **1a** can be oxidized by its photogenerated h^+ to produce a radical cation. Specifically, Fig. S11 presents the contribution maps of the electron, hole, and "electron + hole" during the "$S_0 \rightarrow S_1$" excitation of these two model molecules, as well as the contribution heat maps of non-hydrogen atoms to the hole, electron, and the overlap between the hole and electron, respectively (see details in Table S3). Furthermore, the excited FF-Py-CPP could be effectively quenched by **1a** in accordance with the Stern–Volmer kinetic

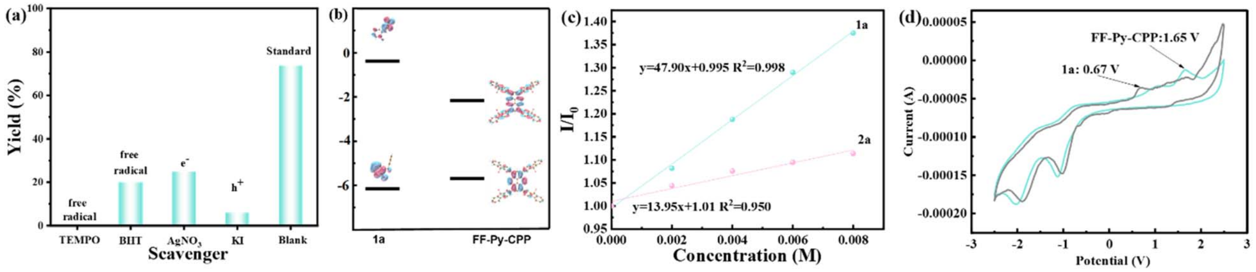

Fig. 4 (a) Controlled scavenger experiments. (b) Calculated energies and electronic charge densities of the HOMO and LUMO of substrate **1a** and FF-Py-CPP. (c) Steady-state emission quenching of FF-Py-CPP with substrates **1a** and **2a**. (d) Cyclic voltammetric analysis of FF-Py-CPP and **1a**.

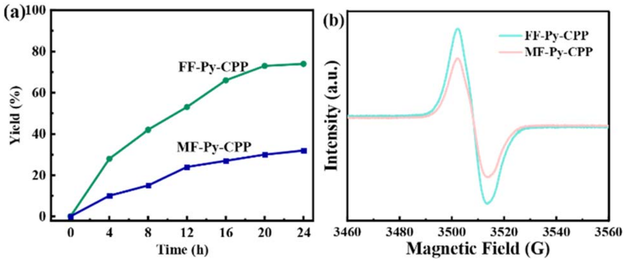

Fig. 5 (a) Time-dependent production of **3a** by FF-Py-CPP and MF-Py-CPP. (b) EPR spectra of FF-Py-CPP and MF-Py-CPP under light.

relationship, while **2a** showed weaker effect (Fig. 4c and S15). These results indicate the SET between FF-Py-CPP* and **1a** is thermodynamically favorable. Cyclic voltammetry (CV) experiments revealed that the oxidative potential of excited FF-Py-CPP ($E_{\text{ox}}^{\text{PC}^*/\text{PC}^{\bullet-}}$ = +1.65 V) is more positive than that of **1a** ($E_{\text{ox}}^{\mathbf{1a}^{\bullet+}/\mathbf{1a}}$ = +0.67 V) (Fig. 4d, see details in the SI).

To determine the effect of catalyst fluorination on photocatalytic performance, the relationship between yield and reaction time was compared for the two catalysts. As shown in Fig. 5, the reaction catalyzed by FF-Py-CPP achieved a yield of 28% in 4 hours and completed within 20 hours. In contrast, the reaction with MF-Py-CPP achieved only 10% yield in 4 hours and remained incomplete after 24 hours. These results demonstrate the superior efficiency of FF-Py-CPP over MF-Py-CPP (Fig. 5a). Besides, the electron spin resonance (EPR) signal of FF-Py-CPP showed the most significant EPR signal intensity under *in situ* visible light irradiation, which suggests that FF-Py-CPP could provide more effective photogenerated electrons in the photocatalytic process (Fig. 5b).

Based on the above experiments and previous literature,[55,64] a plausible reaction mechanism is proposed in Scheme 4. Initially, the FF-Py-CPP achieves effective e^-–h^+ charge separation *via* light irradiation. Subsequently, h^+ oxidizes substrate **1a** to cationic radical intermediate **I**, which generates the radical intermediate **II** after deprotonation. This radical intermediate **II** was trapped by BHT, as detected by HR-MS (Fig. S12). The formation of radical intermediate **I** was further supported by EPR analysis with the spin-trapping agent 5,5-dimethyl-1-pyrroline-*N*-oxide (DMPO) (Fig. S14). Concurrently, e^- reduces persulfate to form SO_4^{2-} and $SO_4^{\bullet-}$. As an efficient hydrogen atom transfer (HAT) agent, the *in situ* generated $SO_4^{\bullet-}$ abstracts $H^\bullet$ from **II** to produce *o*-QM intermediate **III**, which was also confirmed by HR-MS (Fig. S13). Finally, this *o*-QM intermediate reacts with **2a** *via* an IED-HAD process to afford the [4 + 2] cycloaddition product **3a.**

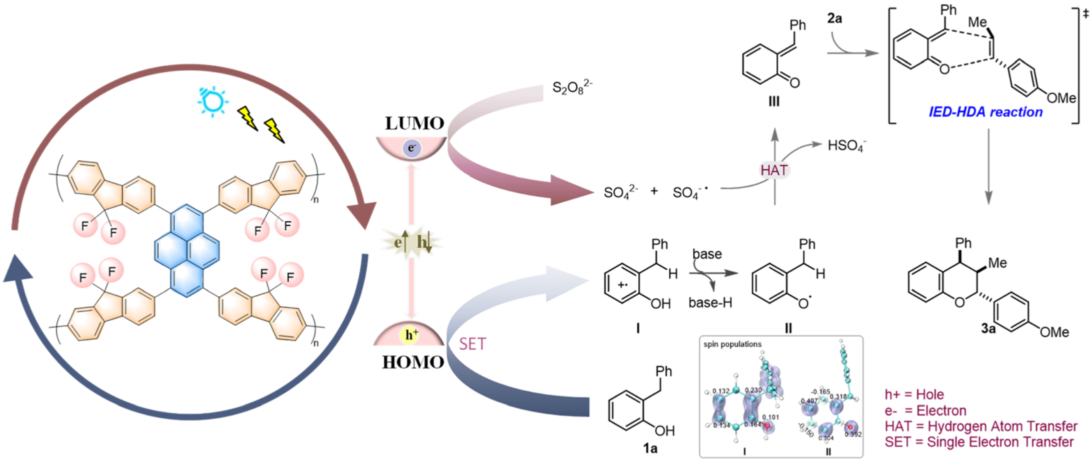

Scheme 4 Proposed reaction mechanism.

Conclusions

In summary, two photoactive CPPs *via* the Suzuki cross-coupling reaction were synthesized, resulting in high-performance metal-free heterogeneous photocatalysts (FF-Py-CPP and MF-Py-CPP). Notably, the CPPs enable effective charge transfer, facilitating successful application as visible-light-activated heterogeneous photocatalysts for *in situ* generation of *o*-QMs *via* sequential SET and HAT processes. This drives subsequent reactions with olefins to form chromane derivatives. Furthermore, these photocatalytic systems are also compatible with the oxidative [3 + 2] cycloaddition of phenols with olefins to construct 2,3-dihydrobenzofurans. These results demonstrate the critical role of FF-Py-CPP in photocatalysis transformations for the synthesis of pharmaceutical and bioactive molecules. This highlights the potential of CPPs to serve as multifunctional catalysts in drug discovery. Additionally, FF-Py-CPP exhibits superior catalytic activity over MF-Py-CPP, demonstrating that the fluoro-substituted fluorene increases the dipole moment and facilitates charge separation, thereby promoting catalytic efficiency. Reusability experiments confirmed the high stability of FF-Py-CPP, proving its potential for industrial applications and contributions to environmental sustainability. We believe that this study could provide insight into the rational design of CPP-based photocatalysts and promote the application of high-performance metal-free heterogeneous photocatalysts across wider organic transformations.

Author contributions

Shuili Liu, Xiu Gu, Shicheng Dong, Nan Huang and Jun Jiang planned the experiments. Shuili Liu and Xingji Liu performed the experiments. All authors contributed to the analysis and interpretation of the data. Lei Shi and Jun Jiang directed the project and wrote the manuscript with contributions from all authors.

Conflicts of interest

The authors declare no competing financial interest.

Data availability

The data supporting this article have been included as part of the supplementary information (SI). Supplementary information is available. See DOI: https://doi.org/10.1039/d5sc08900j.

CCDC 2488731 contains the supplementary crystallographic data for this paper.[68]

Acknowledgements

We acknowledge financial support from the National Natural Science Foundation of China (22161005), and Guangxi Natural Science Foundation (2024GXNSFFA010001 and 2021GXNSFDA075005).

Notes and references

1 S. B. Beil, S. Bonnet, C. Casadevall, R. J. Detz, F. Eisenreich, S. D. Glover, C. Kerzig, L. Næsborg, S. Pullen, G. Storch, N. Wei and C. Zeymer, *JACS Au*, 2024, **4**, 2746–2766.
2 A. Vega-Peñaloza, J. Mateos, X. Companyó, M. Escudero-Casao and L. Dell'Amico, *Angew. Chem., Int. Ed.*, 2020, **60**, 1082–1097.
3 Y. N. Gong, D. C. Zhong and T. B. Lu, *Angew. Chem., Int. Ed.*, 2025, **64**, e202424452.
4 L. Wang and W. Zhu, *Adv. Sci.*, 2023, **11**, 2307227.
5 B. Cai, P. Huang, Y. Fang and H. Tian, *Adv. Sci.*, 2024, **11**, 2308469.
6 A. Cadranel, P. Haines, R. Kaur, A. Menon, P. W. Münich, P. R. Schol and D. M. Guldi, *Adv. Energy Mater.*, 2020, **11**, 2002831.
7 J. Tao, W. Sun and L. Lu, *Biosens. Bioelectron.*, 2022, **216**, 114667.
8 W. Chen, Z. Sun, C. Jiang, W. Sun, B. Yu, W. Wang and L. Lu, *Angew. Chem., Int. Ed.*, 2021, **60**, 16641–16648.
9 A. Savateev, I. Ghosh, B. König and M. Antonietti, *Angew. Chem., Int. Ed.*, 2018, **57**, 15936–15947.
10 X. Li, Y. Chen, Y. Tao, L. Shen, Z. Xu, Z. Bian and H. Li, *Chem Catal.*, 2022, **2**, 1315–1345.
11 N.-Y. Huang, Y.-T. Zheng, D. Chen, Z.-Y. Chen, C.-Z. Huang and Q. Xu, *Chem. Soc. Rev.*, 2023, **52**, 7949–8004.
12 K. Sun, Y. Qian, D. Li and H. L. Jiang, *Adv. Mater.*, 2024, 2411118.
13 W.-K. An, X. Xu, S.-J. Zheng, Y.-N. Du, J. Ouyang, L.-X. Xie, Y.-L. Ren, M. He, C.-L. Fan, Z. Pan and Y.-H. Li, *ACS Catal.*, 2023, **13**, 9845–9856.
14 T. He and Y. Zhao, *Angew. Chem., Int. Ed.*, 2023, **62**, e202303086.
15 Y. Wang, Y. Yang, Q. Deng, W. Chen, Y. Zhang, Y. Zhou and Z. Zou, *Adv. Funct. Mater.*, 2023, **33**, 2307179.
16 G.-F. Liu, Z.-W. Li, Z.-J. Huang, Z. Zhou, Y.-X. Li, A. Huang, Z. Cai, G. Ouyang, B.-H. Ye and Y.-B. Zhang, *J. Am. Chem. Soc.*, 2025, **147**, 1840–1850.
17 J. Xiao, X. Liu, L. Pan, C. Shi, X. Zhang and J.-J. Zou, *ACS Catal.*, 2020, **10**, 12256–12283.
18 D. Taylor, S. J. Dalgarno, Z. Xu and F. Vilela, *Chem. Soc. Rev.*, 2020, **49**, 3981–4042.
19 M. Barawi, L. Collado, M. Gomez-Mendoza, F. E. Oropeza, M. Liras and V. A. de la Peña O'Shea, *Adv. Energy Mater.*, 2021, **11**, 2101530.
20 J. Yu, X. Sun, X. Xu, C. Zhang and X. He, *Appl. Catal., B*, 2019, **257**, 117935.
21 S. Jaiswal, A. Giri, D. Mandal, M. Sarkar and A. Patra, *Angew. Chem., Int. Ed.*, 2023, **62**, e202312910.
22 S. Li, J. Yin, H. Zhang and K. A. I. Zhang, *ACS Appl. Mater. Interfaces*, 2023, **15**, 2825–2831.
23 S. Bhattacharjee, S. Mondal, A. Ghosh, S. Banerjee, A. K. Das and A. Bhaumik, *Small*, 2024, **20**, 2406723.
24 Z. Huang, J. Xian, S. Lv, S. Xu, J. Li, F. Xie and B. Li, *Org. Lett.*, 2023, **25**, 7974–7978.

25 X. Luo, S. Zhou, S. Zhou, X. Zhou, J. Huang, Y. Liu, D. Wang, G. Liu and P. Gu, *Adv. Funct. Mater.*, 2024, **35**, 2415244.

26 H. Ali, Y. Orooji, A. Y. A. Alzahrani, M. H. Al Mughram, A. M. Abu-Dief, I. Omar, A. Hayat, D. Yue and Y. Xu, *Coord. Chem. Rev.*, 2025, **543**, 216884.

27 S. Qiao, M. Di, J.-X. Jiang and B.-H. Han, *EnergyChem*, 2022, **4**, 100094.

28 P. Dong, H. Lv, R. Luo, Z. Li, X. Wu and J. Lei, *Chem. Eng. J.*, 2023, **461**, 141817.

29 X. Zhao, S. Shang, H. Liu, C. Peng and J. Hu, *Chemosphere*, 2024, **356**, 141947.

30 Y. Zhang, J. Zhang, S. Dou, H. Shang, J. Xu, Y. Dong, Y. Zhang, Y. Lou, C. Pan and Y. Zhu, *Angew. Chem., Int. Ed.*, 2025, e202512844.

31 Y. J. Chen, J. Z. Zhang, Z. X. Wu, Y. X. Qiao, L. Zheng, F. Wondu Dagnaw, Q. X. Tong and J. X. Jian, *Angew. Chem., Int. Ed.*, 2023, **63**, e202318224.

32 F. Xu, S. Yang, G. Jiang, Q. Ye, B. Wei and H. Wang, *ACS Appl. Mater. Interfaces*, 2017, **9**, 37731–37738.

33 H. Chen, Z. Yang, C. L. Do-Thanh and S. Dai, *ChemSusChem*, 2020, **13**, 6182–6200.

34 D. Yuan, M. A. Awais, V. Sharapov, X. Liu, A. Neshchadin, W. Chen and L. Yu, *J. Am. Chem. Soc.*, 2021, **143**, 5239–5246.

35 J. Qian, Q. Lu, F. Xu, L. Chen and J. Xia, *J. Hazard. Mater.*, 2021, **410**, 124544.

36 A. Hori, A. Matsumoto, J. Ikenouchi and G.-i. Konishi, *J. Am. Chem. Soc.*, 2025, **147**, 9953–9961.

37 H. Bin, Y. Yang, Z. Peng, L. Ye, J. Yao, L. Zhong, C. Sun, L. Gao, H. Huang, X. Li, B. Qiu, L. Xue, Z. G. Zhang, H. Ade and Y. Li, *Adv. Energy Mater.*, 2017, **8**, 1702324.

38 L. Li, W.-y. Lo, Z. Cai, N. Zhang and L. Yu, *Macromolecules*, 2016, **49**, 6903–6909.

39 K. C. Ranjeesh, A. Rezk, J. I. Martinez, S. Gaber, A. Merhi, T. Skorjanc, M. Finšgar, G. E. Luckachan, A. Trabolsi, B. R. Kaafarani, A. Nayfeh and D. Shetty, *Adv. Sci.*, 2023, **10**, 2303562.

40 Z. Xu, W. Dong, X. Cui and Q. Duan, *Chemosphere*, 2024, **355**, 141801.

41 X. Dong, F. Zhang, F. Huang and X. Lang, *Appl. Catal., B*, 2022, **318**, 121875.

42 C. Han, S. Xiang, S. Jin, C. Zhang and J.-X. Jiang, *ACS Catal.*, 2022, **13**, 204–212.

43 Y. Yang, Y. Wang, Y. Gao, J. Zhou, D. Zhu, T. Wang, X. Zhang, L. Tang and Y. Zhou, *Appl. Catal., B*, 2026, **380**, 125778.

44 K. Yu, S. Bi, W. Ming, W. Wei, Y. Zhang, J. Xu, P. Qiang, F. Qiu, D. Wu and F. Zhang, *Polym. Chem.*, 2019, **10**, 3758–3763.

45 W.-J. Bai, J. G. David, Z.-G. Feng, M. G. Weaver, K.-L. Wu and T. R. R. Pettus, *Acc. Chem. Res.*, 2014, **47**, 3655–3664.

46 T. N. Purdy, B. S. Moore and A. L. Lukowski, *J. Nat. Prod.*, 2022, **85**, 688–701.

47 X. Li, Z. Li and J. Sun, *Nat. Synth.*, 2022, **1**, 426–438.

48 A. Maestro and M. Zurro, *Org. Biomol. Chem.*, 2023, **21**, 8244–8258.

49 C. Bi, H. Liu, R. She, Y. Fan, G. Chen and Y. Peng, *Org. Lett.*, 2025, **27**, 8846–8850.

50 Y. Hoshino, K. Tanaka, S. Nohara, S. Iwai, N. Yamaguchi, Y. Asada, Y. Kamiyama and Y. Tanaka, *Synlett*, 2023, **34**, 2525–2529.

51 Y. Y. Liu, X. Y. Yu, J. R. Chen, M. M. Qiao, X. Qi, D. Q. Shi and W. J. Xiao, *Angew. Chem., Int. Ed.*, 2017, **56**, 9527–9531.

52 D. Liang, L.-P. Tan, W.-J. Xiao and J.-R. Chen, *Chem. Commun.*, 2020, **56**, 3777–3780.

53 F. Zhou, Y. Cheng, X.-P. Liu, J.-R. Chen and W.-J. Xiao, *Chem. Commun.*, 2019, **55**, 3117–3120.

54 M. Uyanik, K. Nishioka, R. Kondo and K. Ishihara, *Nat. Chem.*, 2020, **12**, 353–362.

55 S. Wang, G. Liang, C. Wang, C.-H. Wang, Z. Huang, C.-H. Tung and L.-Z. Wu, *Org. Lett.*, 2024, **27**, 470–475.

56 K. Gebauer, F. Reuß, M. Spanka and C. Schneider, *Org. Lett.*, 2017, **19**, 4588–4591.

57 L.-N. Gao, K. Zheng, H.-Y. Chen, Y.-N. Gao, Z.-Z. Li, C. He, S.-H. Huang, R. Hong, M. Bian and Z.-J. Liu, *Org. Biomol. Chem.*, 2025, **23**, 2775–2792.

58 Q. Hou, X. Liu, L. Chen, R. Cao, S. Yue, L. Zhu and B. Xiong, *Curr. Org. Chem.*, 2025, **29**, 1221–1239.

59 K. Zhang, X. Dong, B. Zeng, K. Xiong and X. Lang, *J. Colloid Interface Sci.*, 2023, **651**, 622–632.

60 X. Gao, C. Shu, C. Zhang, W. Ma, S.-B. Ren, F. Wang, Y. Chen, J. H. Zeng and J.-X. Jiang, *J. Mater. Chem. A*, 2020, **8**, 2404–2411.

61 B. He, Z. Wang, P. Xiao, T. Chen, J. Yu and L. Zhang, *Adv. Mater.*, 2022, **34**, 2203225.

62 C. Qu, L. Chen, P. Wang, J. Zhang, Y. Ding, X. Long, T. Zhang, Y. Zhao and J. Deng, *J. Am. Chem. Soc.*, 2025, **147**, 6739–6746.

63 X. Yan, X. Jia, Z. Luo, S. Ji, M.-J. Zhang, H. Zhang, M. Yu, J. Orts, K. Jiang, Z. Lin, Z. Deng, X.-D. Kong, B. Kobe, Y.-L. Zhao, M. Mobli and X. Qu, *Nat. Chem.*, 2025, **17**, 1058–1066.

64 P. T. Parvatkar, S. Kandambeth, A. C. Shaikh, I. Nadinov, J. Yin, V. S. Kale, G. Healing, A.-H. Emwas, O. Shekhah, H. N. Alshareef, O. F. Mohammed and M. Eddaoudi, *J. Am. Chem. Soc.*, 2023, **145**, 5074–5082.

65 T. R. Blum, Y. Zhu, S. A. Nordeen and T. P. Yoon, *Angew. Chem., Int. Ed.*, 2014, **53**, 11056–11059.

66 N. L. Reed and T. P. Yoon, *Chem. Soc. Rev.*, 2021, **50**, 2954–2967.

67 Z. Chen, M. Pitchakuntla and Y. Jia, *Nat. Prod. Rep.*, 2019, **36**, 666–690.

68 CCDC 2488731: Experimental Crystal Structure Determination, 2026, DOI: 10.5517/ccdc.csd.cc2pjqnm.